# IMPACT OF SHAPE CHANGE ON CAPSULE AERODYNAMICS AND SHOCK-WAVE BOUNDARY LAYER INTERACTION

*Thomas Gawehn, Thorn Schleutker, Ali Gülhan*

German Aerospace Center (DLR), Institute of Aerodynamics and Flow Technology,
51147 Cologne, Germany

## ABSTRACT

Blunt capsule shapes have proven to be suitable for atmospheric entry flights on numerous missions. Some concepts like MarcoPolo-R focus on fully passive entry systems without a parachute, demanding for aerodynamic stability of the shape throughout the complete entry flight. These probes are commonly equipped with a Thermal Protection System (TPS) consisting of an ablative material. The recession of the TPS in the early entry flight phase may lead to a significant shape change. The capsule needs to remain aerodynamically stable for a successful mission completion despite these shape changes.

Within ESA's Modshape TRP the aerodynamic impact of the recession on the MarcoPolo-R capsule is investigated experimentally and numerically. Static force and moment measurements in the TMK wind tunnel are a major part of this TRP. The experimental simulations are conducted on the nominal or baseline configuration and two configurations representing the aero shape with the recessed TPS after the hot entry flight phase of different entry scenarios.

The flow structure around the capsule is visualised at supersonic Mach numbers by means of schlieren imaging. Under certain conditions, development of a complex shock system on the leeward side of the inclined capsule is observed. Numerical simulations with the DLR TAU code are performed to support the interpretation of the flow phenomena in these cases.

***Index Terms*** **—** Planetary probe; atmospheric entry flight; capsule aerodynamics; schlieren visualization; computational fluid dynamics (CFD); secondary shock structures; shock wave boundary layer interaction (SBLI)

## 1. INTRODUCTION

The most critical part of an Earth return or exploration mission is the entry flight, in which the high kinetic and potential energy of a spacecraft are dissipated. Blunt geometries are commonly chosen for the aerodynamic outer shell. These shapes generate high drag, which allows the probe to quickly decelerate to the terminal velocity and also minimizes the total heat load.

Blunt capsule shapes have proven to be suitable for atmospheric entry flight despite having low aerodynamic stability in the transonic and subsonic flow regimes. Concepts like the MarcoPolo-R capsule, which is based on a modified Hayabusa shape, focus on fully passive entry systems without a parachute. They therefore demand for aerodynamic stability throughout the complete entry flight trajectory. The desired aerodynamic behaviour of the capsule was confirmed experimentally and numerically within the frame of ESA's MarcoPolo-R Earth Re-Entry Capsule Dynamic Stability Characterization TRP [1].

The MarcoPolo-R capsule geometry was selected as baseline configuration for the ESA TRP Modshape (Modelling Capsule Stability accounting for Shape Change) in 2019. The main goal of the Modshape project is to experimentally quantify the impact of the change of the outer mold line caused by the recession of the TPS on the flight qualities of the capsule [2].

Within the project, wind tunnel tests were performed in the trisonic wind tunnel TMK of DLR in Cologne to determine the static aerodynamic behaviour of the virgin capsule and two configurations that represent the aero shape after TPS recession for different entry scenarios. A Mach number range of $0.5 \leq M \leq 3.0$ is covered in the experiments.

Earlier tests on the MarcoPolo-R aero shape revealed the occurrence of shock-wave boundary-layer interaction on the leeward side of the inclined capsule at free stream Mach numbers of $1.3 \leq M \leq 1.5$. This phenomenon was investigated experimentally and numerically and interpreted with reference to literature [3]. Within the Modshape TRP the shock-wave boundary-layer interaction could be reproduced for the virgin capsule's geometry. The small changes to the shape of the aeroshell applied in case of the two geometries considering the TPS recession resulted in significantly different flow structures. This publication addresses the analysis of the aerodynamic impact of the shape change and the investigation of the differences in the flow structure at a test Mach number of $M = 1.5$.

## 2. EXPERIMENTAL TOOLS

### 2.1. Trisonic Wind Tunnel Cologne (TMK)

The TMK facility is a trisonic blow down wind tunnel with a rectangular test section of 0.6 m $x$ 0.6 m. Air from a pressure reservoir passes a storage heater and a settling chamber and is then accelerated through the adaptable de Laval nozzle. In the test section, the flow conditions are nearly constant. The flow is decelerated downstream in the diffuser system. Depending on Mach and Reynolds conditions, a maximum testing time of up to 60 seconds is achieved.

The standard Mach number range in the supersonic operation mode is $1.25 < M < 4.5$. The wind tunnel is operated at a dynamic pressure of $q_\infty \approx 1$ bar in this range. The Mach number is set by adapting the nozzle. Tests with a reduced dynamic pressure and Mach numbers up to $M = 5.7$ can be realized by ejecting additional air mass flow downstream the subsonic diffuser. If necessary, the flow can be heated by the storage heater.

For Mach numbers of $0.5 < M < 1.2$, an additional transonic test section with perforated walls of variable aperture is installed downstream the supersonic test section. In this case, the wind tunnel is operated at a static pressure of $p_\infty \approx 1$ bar and the Mach number is controlled via the adaptable diffuser downstream the test section.

### 2.2. Wind tunnel models

Figure 1 shows the reference aero shape of MarcoPolo-R with its diameter of 880 $mm$ and the $CAD$-design of the baseline wind tunnel model for TMK tests (scale 1: 11). This baseline model (S1) has a diameter of $D_{Ref\_S1} = 80$ mm and represents the aero shape of the virgin capsule. Two further shapes are tested that represent either a capsule with axially symmetric TPS recession (S2) with a diameter of $D_{Ref\_S2} = 77.8$ mm or an asymmetrically deformed shape (S3) with an average diameter of $D_{Ref\_S3} = 77.67$ mm. The reference surface of all shapes is calculated as $S_{Ref} = \pi/4 \cdot D_{Ref}^2$.

The definition of the deformed shapes is based on the recession measured on a Camphor model after wind tunnel tests. These tests were performed in the H2K facility at $M = 6.0$, $Re = 5.4 \cdot 10^6$ and $\alpha = 0°$ angle of incidence for S2 and $\alpha = 5°$ for S3. Further details on the performed recession tests in H2K and the measured ablated shapes are presented by Seltner et al. [4].

The Moment Reference Centre ($MRC$) is defined on the centreline of each capsule and $0.25 \cdot D_{Ref}$ downstream the stagnation point at an angle of incidence of zero degrees. If the centre of gravity ($CoG$) coincides with the $MRC$, the pitching moment curves provide a direct reference to the static aerodynamic stability of the capsule.

For the reference aero shape, the existing wind tunnel model of MarcoPolo (MP) is used. It was made of a high strength Aluminium alloy (3.4345) and coated with a 30 ± 3 µm nickel layer. The models for S2 and S3 are made from the stainless steel Ramax HH (1.2085). The geometry of all three models is validated with the optical high-precision profilometer Keyence $VR - 5200$.

The wind tunnel models are designed with a smooth front surface. They are fixed to the balance via an adapter and screws on their leeward side. The balance is connected to a Ø 18 mm sting and covered by a shell with Ø 22 mm. For the baseline configuration, the sting to capsule diameter ratio is $D_S/D_{Ref\_S1} = 0.275$ and the sting length to capsule diameter ratio is $L_S/D_{Ref\_S1} = 3.39$. An inner and outer clearance of 1 mm between shell and model allows for contact-free measurements at all incidence angles, even if aerodynamic loads lead to a slight bending of the sting-balance-system.
The photographs in Figure 2 show the front and rear of the three capsules.

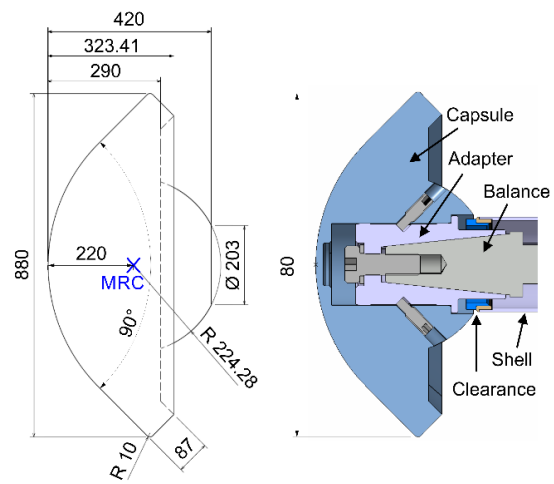


**Figure 1: Reference aero shape (left) and wind tunnel baseline model (S1, Ø 80 mm) (right)**


**Figure 2: Photographs of MP/S1, S2 and S3 model**

### 2.3. Static Aerodynamic Measurements

Aerodynamic coefficients are determined with the six-component strain gauge balance $DLR - 0007$. A balance of Ø 18 mm is chosen as a compromise between the gages capability to withstand and measure the expected axial loads and a small model to shell diameter ratio. The distance between the two instrumented sections of the balance for longitudinal and lateral measurements is 100 mm.

The base pressure downstream the model is measured relative to ambient pressure with a $PDCR$ 22 sensor, which is positioned outside the test section. The sensor is connected via a long, thin tube (Ø 1.6 $x$ $L$ 2500 mm) guided along the model support system and sting to a pressure port inside the shell (see Figure 1). The pressure level is assumed to be representative for an average pressure distribution on the model's base. In addition, three thin pressure tubes connected to Kulite pressure sensors are installed outside the shell to allow for pressure measurements in the base cavity. These tubes are visible in the schlieren images. They end near the model surface and have been proven to not influence the aerodynamic measurements.

The pressure, temperature, angle of incidence and balance data is recorded synchronized and with an acquisition rate of 100 Hz. In static aerodynamic measurements, a filter of 10 Hz is applied. Raw data is stored during the test together with calibration information. Post-processing is performed after the test with an in-house developed tool.

### 2.4. Flow Visualisation

The schlieren visualisation for supersonic tests in TMK uses a Z-arrangement with a vertical knife edge. The images are recorded with a monochromatic PROSILICA $GE4000$ camera (Frame rate: up to 5 Hz at full resolution, minimum exposure time: 140 µs, sensor: $CCD$, res.: $4008x2672$ px, bit depth: 16 bit). With this line-of-sight method, the three-dimensional flow structures are visualised in two dimensions. The density gradients are integrated along the line of sight (i.e. perpendicular to the graph).

## 3. EXPERIMENTAL TEST CAMPAIGN

The test campaign consisted of a total of 26 tests in TMK and 25 preceding tests in H2K.

### 3.1. Test Procedure

For minimizing the loads on the balance in aerodynamic tests, the models are aligned at $\alpha = 0°$ for wind tunnel start-up and shut-down. After a short transitional phase of the tunnel, data is recorded at constant flow conditions. The model is continuously swept in the range of $-2.5° \leq \alpha \leq +25°$ at a rate of $2°/s$ in both directions. A dependency of the aerodynamic data on the sweep direction is not observed. Though, at the low-pressure levels during the supersonic tests, the base pressure measurement inside the shell reacts with short delay to sudden pressure changes in the flow field. This is, for example, the case during the wind tunnel start-up. The delay is caused by the unavoidable length of the tube. The data presented in this paper is taken from the sweep-down phase to circumvent the problem.

High quality schlieren images are recorded in full resolution at 3 Hz and 1 ms exposure time during the supersonic tests. As previous investigations on the baseline geometry showed [3], oscillations of the shock structures that form on the leeward side of the inclined capsule can be neglected at that exposure time.

### 3.2. Test Conditions

The Mach- and Reynolds-conditions of the experiments considered in this paper are plotted in Figure 3. That graph also shows the trajectory of the sample return capsule used as reference in the Modshape project. The transonic tests at Mach numbers $0.5 \leq M \leq 0.95$ can only be performed at a static pressure of $p_\infty \approx 1$ bar. Thus, the predicted flight Reynolds number cannot be reproduced in that range. The supersonic tests are conducted at reduced stagnation pressures using the ejector system of the TMK wind tunnel. This allows rebuilding of the trajectory in the range $1.5 \leq M \leq 3.0$. Additional tests were conducted in the H2K facility at $M = 6.0$ using models with a diameter of $D_{Ref\_H2K} = 0.1$ m. These tests were performed at the nominal and a reduced Reynolds number [4]. Camphor models were used to analyse the cold recession during the wind tunnel test. Based on the results of selected tests at nominal condition the shapes of the deformed capsule models S2 and S3 were defined.

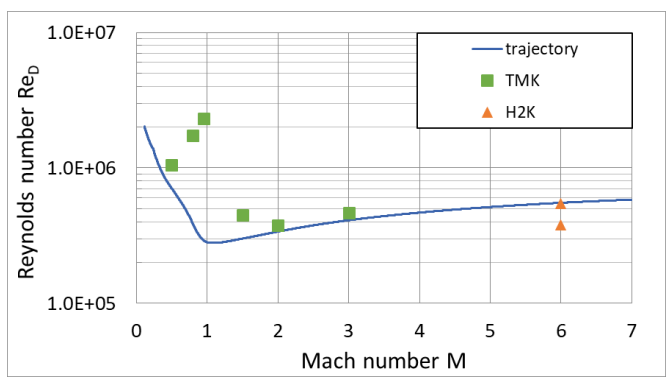


**Figure 3: Test conditions and flight trajectory**

### 3.3. Coordinate System

The coordinate system is given in Figure 4. It is used for definition of the aerodynamic coefficients. Its origin lies in the capsule's $MRC$. At zero-degree angle of incidence and

yaw angle, the x-axis points in opposite direction of the flow. The z-axis is defined positive in direction of the gravitation vector and the y-axis is oriented according to the right-hand rule.

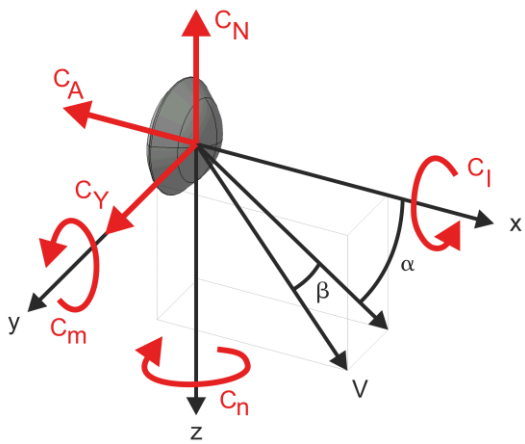


**Figure 4: Aerodynamic coordinate system**

## 4. EXPERIMENTAL RESULTS

### 4.1. Aerodynamic Coefficients of Configuration S1

The charts in Figure 5 show data of tests with the baseline capsule model ($D_{Ref\_S1} = 80$ mm) plotted against the incidence angle $\alpha$. The data sets are grouped in transonic tests (a, b) and supersonic tests (c, d). The experimental uncertainties are shown in black as vertical error bars. They were calculated from the partial derivatives applying the Gaussian error propagation rule. For details of the uncertainty estimation see [3].

At all Mach numbers the axial force coefficient $C_A$ is highest at $\alpha = 0°$ and decreases with increasing angle of incidence. In the subsonic range, the level of $C_A$ increases with Mach number (a). At supersonic conditions this trend is reversed (c). A region of nearly constant $C_A$ can be observed for $\alpha \leq 8°$ at $M = 1.5$. In this range, the axial force coefficient is smaller than in the test at the higher Mach number $M = 2.0$.

The axial force coefficient can be divided into a fore body part and a base part:

$$C_A = C_{A_{FB}} + C_{A_B},$$

whereby the base part is calculated from the base pressure coefficient as

$$C_{A_B} = -C_{p_B} \cdot \frac{S_B}{S_{Ref}}$$

considering the ratio of the base area $S_B$ to the reference area $S_{Ref}$.

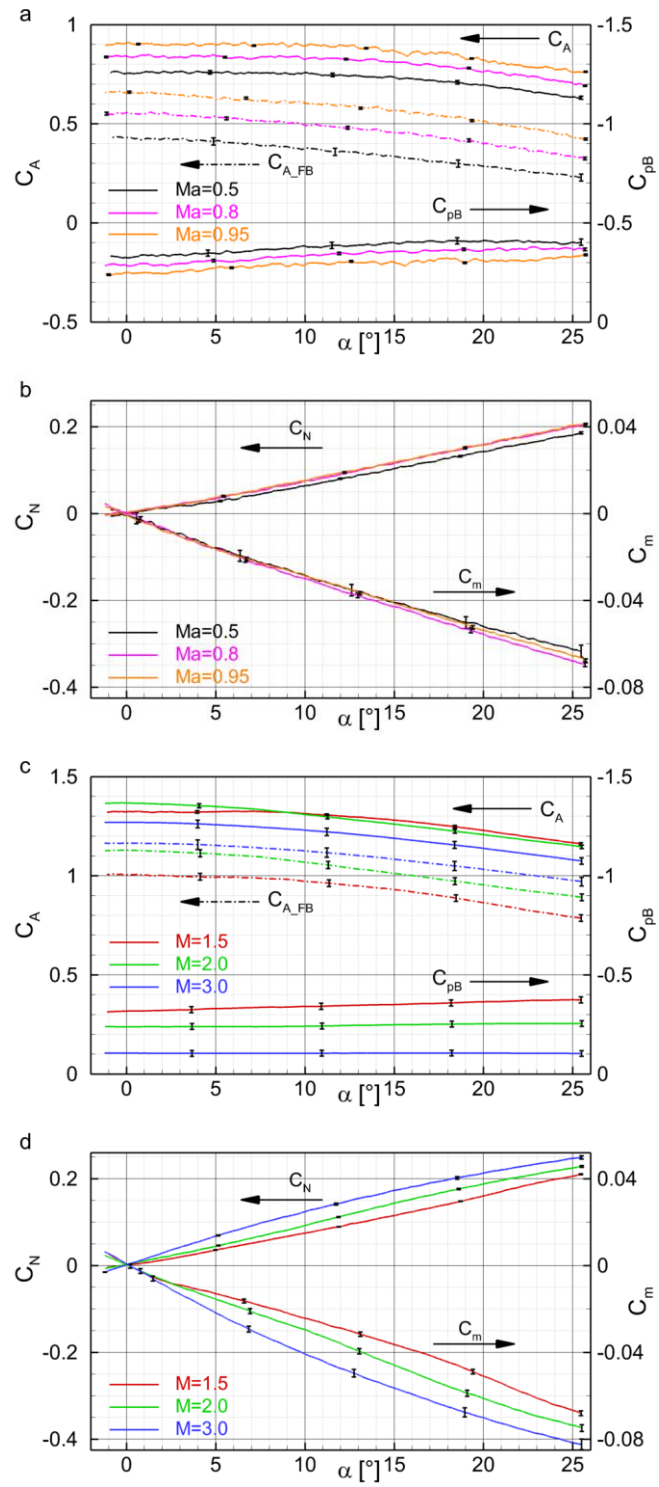


**Figure 5: Aerodynamic coefficients of configuration S1: Axial force $C_A$, base pressure $C_{p_B}$, axial fore body force $C_{A_{FB}}$, normal force $C_N$ and pitching moment $C_m$**

The corresponding coefficient $C_{p_B}$ is shown with reversed ordinate axis direction. The plotted base pressure is the measurement inside of the shell. It is assumed to be representative for the average pressure on the capsule's rear. In this study, the base pressure coefficient is negative by definition and increases with the Mach number. All curves show a slight decrease when the angle of incidence is increased except for $M = 3.0$ where the coefficient is almost constant. The uncertainties shown in the graphs amount to several percent, especially at supersonic conditions where the pressure levels are low.

The axial fore body force coefficient $C_{A_{FB}}$ is calculated according to the above equations for an area ratio of $S_B/S_{Ref} = 1$. Similar to $C_A$, the coefficient $C_{A_{FB}}$ is highest around $\alpha = 0°$ and decreases with increasing angle of incidence. Apart from small deviations, the shape of the curves is comparable across the plotted Mach numbers. The curve shifts to a higher level when the Mach number is increased. An exception is $M = 1.5$. In this case $C_{A_{FB}}$ is almost constant for$\alpha \leq 8°$, as has been observed for $C_A$.

The change of the base pressure with the Mach number leads to the reversed trend in $C_A$ in the supersonic range. By reducing $C_A$ to $C_{A_{FB}}$, thus removing the base pressure's influence, this trend is eliminated.

At all investigated Mach numbers, the normal force coefficient $C_N$ is zero at $\alpha = 0°$ and increases with incidence angle and test Mach number. Depending on the Mach number different curve characteristics are observed. In the subsonic regime, $C_N$ shows a rather small positive gradient $dC_N/d\alpha$ at zero degrees angle of incidence. This gradient increases with the angle up to $\alpha \approx 15°$ and stays nearly constant at higher angles. The normal force coefficient seems independent of the Mach number in the range $0.8 \leq M \leq 0.95$. In contrast, for $M = 3.0$, the initial gradient is higher than in the subsonic flow, but continuously decreases with increasing $\alpha$. In the range of $1.5 \leq M \leq 2.0$ the curves start at the origin with a positive second derivative $d^2C_N/d\alpha^2$, then pass a turning point ($\alpha \approx 20°$, $11°$, respectively) before the second derivative turns negative.

For the symmetrical capsule all curves show a pitching moment coefficient $C_m$ that is zero at $\alpha = 0°$ and then decreases with increasing incidence angle. This gives the capsule a statically stable aerodynamic behaviour in the investigated Mach number range (assuming $MRC = CoG$). In the subsonic regime ($M \leq 0.95$), the Mach number dependency of $C_m$ is small. This leads to comparable values at different Mach numbers up to an incidence angle of $\alpha \approx 7°$. Above that angle, the capsule's stability increases when Mach number is changed from $M = 0.5$ to $M = 0.8$, but slightly decreases again, when it is changed to $M = 0.95$.

In the supersonic flow at $M = 3.0$ the absolute value of the gradient $|dC_m/d\alpha|$ is initially higher than in subsonic, but constantly decreases with increasing angle of incidence. In the range of $1.5 \leq M \leq 2.0$ the gradient's amount is initially smaller or comparable to the subsonic cases, but changes tendency twice giving two turning points on each curve ($\alpha = 8.0°/21.4°$ and $6.7°/14.6°$, respectively).

The above analysis for the baseline geometry reveals the change in the capsule's aerodynamic behaviour when decelerating from supersonic to subsonic conditions and thereby underlines the necessity of performing experiments in the complete Mach number range experienced by the capsule during the entry flight.

### 4.2. Impact of Shape Change on Aerodynamic Coefficients at $M = 1.5$

The shift of the $CoG$ induced by the recession of the TPS was analysed numerically within the Modshape project. For both deformed capsule shapes (S2 and S3) the $CoG$ shift is in the order of 1 % in backward direction. This causes a decreased static stability. Nonetheless, within analysis of the experimental data, the three capsule shapes are treated as independent geometries with the given reference diameters $D_{Ref}$ and the $MRC$s at $0.25 \cdot D_{Ref}$.

Figure 6 shows the aerodynamic coefficients for all three capsule shapes at a test Mach number of $M = 1.5$. The deformed shapes S2 and S3 experience a lower axial force coefficient $C_A$ than the baseline shape S1. The same accounts for the fore body force coefficient $C_{A_{FB}}$ as the base pressure coefficient $C_{p_B}$ hardly differs.

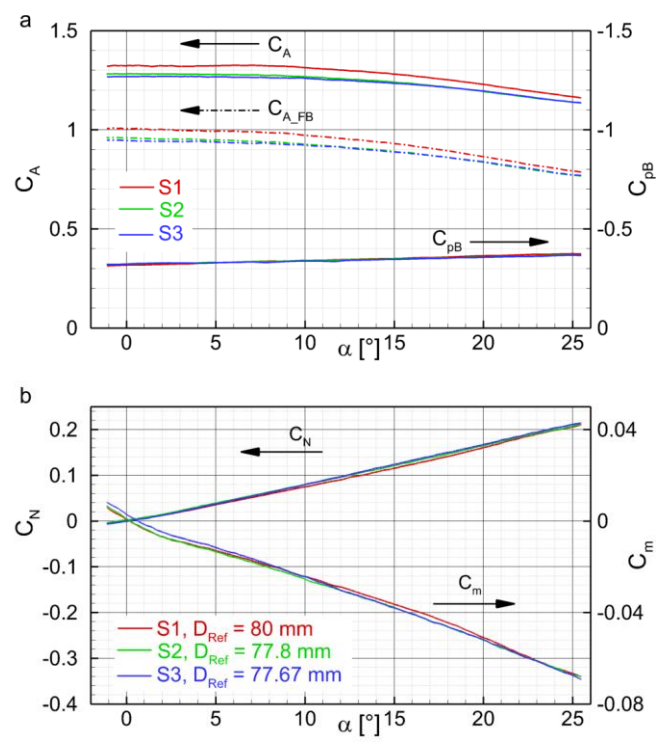


**Figure 6: Aerodynamic coefficients at $M = 1.5$: Axial force $C_A$, base pressure $C_{p_B}$, axial fore body force $C_{A_{FB}}$, normal force $C_N$ and pitching moment $C_m$**

A further analysis of the impact of the shape change on the aerodynamic coefficients based on the plots in Figure 6 is hardly possible. Therefore, additional plots showing the differences in the coefficients between deformed shapes and the baseline shape are created by application of Savitzky-Golay filter to test data (side points: 100, polynomial order: 1) with extraction of one data point per half degree (closest point method) and subsequent calculation of differences ($\Delta C = C_{S2,S3} - C_{S1}$).

The result of this procedure is shown in Figure 7. The differences in the coefficients are small and partly in the range of the measurement uncertainty. Nonetheless, the tendencies provide valuable information about the impact of the shape change on the aerodynamics.

Both deformed capsule shapes lead to a reduced fore body force coefficient. The impact of the S3 configuration is more pronounced at low angles of incidence. Since the coefficients are based on the respective actual diameter of the capsules, the decrease is not caused simply by the reduction in projected area but rather by a modification of the front shield shape and / or pressure distribution.

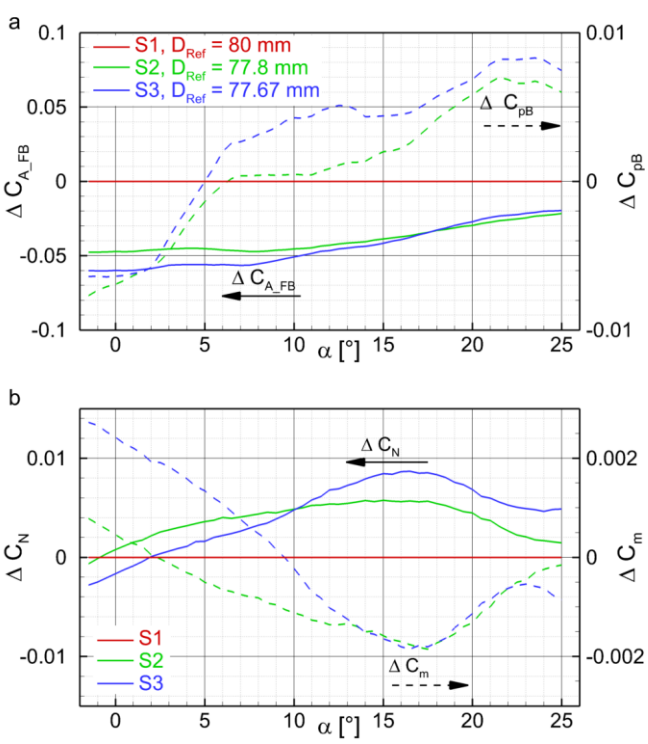


**Figure 7: Shape dependent deviation $\Delta C$ of aerodynamic coefficients at $M = 1.5$**

The base pressure deviation from the original is small, negative at low angles of incidence and then turns positive with increasing $\alpha$. S2 represents a symmetrically deformed shape, so the small offset of $C_N$ and $C_m$ at $\alpha = 0°$ is a result of the combined uncertainty of the measurement, including model asymmetries due to manufacturing, model alignment, force measurement and run-to-run uncertainties. The asymmetrical shape of S3 leads to a higher offset of both coefficients at $\alpha = 0°$.

The pitching moment coefficient $C_m$ of S2 and S3 coincides in the range $13° \leq \alpha \leq 23°$, but deviates at higher and lower angles. The normal force coefficient $C_N$ of S3 is smaller than that of S2 at low angles of incidence. They yield similar values around $\alpha = 10°$. Beyond that angle, the offset between the two curves changes the sign. $C_N$ is higher in case of the deformed shapes S2 and S3 than the coefficient of the virgin capsule's shape S1.

### 4.3. Aerodynamic Impact of Shape Change at different Mach numbers

The three capsule shapes experience different aerodynamic coefficients on the same $\alpha$-polar and Mach number, as has been shown in the previous section exemplarily for $M = 1.5$. As the experiments at different Mach numbers further demonstrated, the impact of the shape change on the aerodynamic coefficients also changes with Mach number. To demonstrate this, Figure 8 shows the aerodynamic coefficients for the three capsule shapes at an arbitrarily chosen incidence angle of $\alpha = 10°$ plotted over the Mach number.

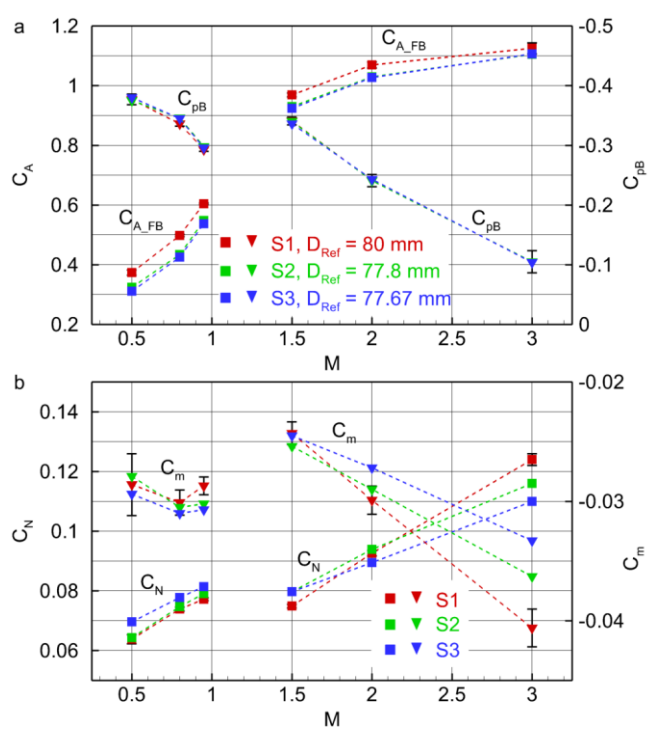


**Figure 8: Aerodynamic coefficients over Mach number for an incidence angle of $\alpha = 10°$**

The axial forebody force coefficient $C_{A\_FB}$ of all three shapes increases with Mach number. S1 has the highest $C_{A\_FB}$ coefficients. The shape S2 yield slightly higher $C_{A\_FB}$ than S3 in subsonic and low supersonic regimes, but equal values for $M \geq 2.0$. A variation in the base pressure coefficient $C_{pB}$ between the three shapes is only observed in subsonic flow and the differences are below the measurement uncertainty.
The normal force coefficient $C_N$ of all three shapes increases with Mach number. In subsonic flow, S1 and S2 yield very similar coefficients that are lower than those of S3. At supersonic Mach numbers, $C_N$ is lowest for S1 at M=1.5 but shows the highest growth with the Mach number. S2 and S3 show similar values at $M = 1.5$ but the gradient $\partial C_N / \partial M$ is higher for S2.

The pitching moment coefficient $C_m$ at $\alpha = 10°$ is always negative. As shown in the plot, the uncertainty on $C_m$ is relatively high at $M = 0.5$ and interpretation of the measured coefficients at that Mach number is not justified. The lowest values in the subsonic tests are found at $M = 0.8$. At this condition, S1 experiences the smallest absolute value of $C_m$, followed by S2 and S3. At $M = 0.95$, the absolute value of $C_m$ decreases for S1, but stays almost constant for S2 and S3.

In the supersonic cases, S1 and S3 show almost the same values at $M = 1.5$ and the data point for S2 is found below. Above that Mach number, S1 experiences the highest negative gradient $\partial C_m / \partial M$ whereby the curves for S2 and S3 show almost the same negative trend.

## 5. NUMERICAL REBUILDING

In the previous project MarcoPolo-R, a complex interaction between the leeward shock system and the boundary layer was observed on the surface of the virgin capsule. This interaction was further investigated for the Mach number $M = 1.5$ and the experiments at this Mach number were rebuilt numerically to assist the interpretation of the observed phenomena [3]. In this work, comparable simulations are performed on the aero shapes of the post-flight shapes S2 and S3 using the same 2016 version of DLR's flow solver TAU [5, 6]. The recent and former numerical results are compared against the aerodynamic coefficients determined in the experiments.

The TAU code applies the finite volume method to the Navier-Stokes equations. It uses structured, unstructured and hybrid grids. Several one and two equation turbulence models as well as Reynolds stress and DES models are available in the flow solver for simulation of turbulent flows. Laminar and inviscid simulations can be conducted using TAU, too. Besides the perfect gas, real gases as well as reacting flows in equilibrium and chemical and/or thermal non-equilibrium can be simulated. The TAU code provides different techniques for convergence acceleration, such as local time stepping and multigrid approaches.

### 5.1. Computational Domain

In this work, hybrid grids with 13 prism layers are generated for each capsule shape via the CENTAUR grid generation software. The prism layers allow sufficient resolution of the boundary layer while keeping the computational costs in an acceptable range. The thickness of the prism layers is not adjusted during the calculation. Instead, it is configured before the simulations such that the requirements of the used SST turbulence model are met. Though, the adaptation routine implemented in TAU is used for local refinement of the mesh to better resolve the shock structures. The grids are also pre-refined in the region of interest. The symmetry of the test setup is used to reduce the numerical effort by cutting the flow field in half.

The sting holding the sample in the wind tunnel experiments is included in the numerical grid. The connection between sting and model is simplified as a 1 mm gap.

The initial grids have a total of $18 - 20$ million cells and $3 - 4$ million vertices. The grids are adapted during the simulation to roughly 60 million cells and 12 million vertices. The exact numbers vary with the aeroshell geometry and simulation run.

The sensitivity of the solution to the grid resolution was assessed in the previous study by reducing the grid size [3]. It was found that a coarser grid did not impact the aerodynamic coefficients. The general use of the fine grid was justified by the interest in the secondary shock system. This shock system has a minor influence on the coefficients. Nevertheless, the shock system requires a high grid resolution for being resolved. Accordingly, the fine grid is also used in this study.

### 5.2. Visualisation of Numerical Solutions

The commercial TECPLOT software is used to visualise the numerical results. TECPLOT allows the investigation of most flow properties and effects, including the visualisation of surface tension lines. However, the software does not provide the necessary functionality to generate schlieren images. Thus, a tool that is developed in-house is used for this purpose: the NICE program (*Numerical Images for Comparison with Experiments*).

NICE is dedicated to the calculation of schlieren images from numerical data. The program considers the experimental boundary conditions, such as the orientation and the type of the knife edge. The major simplification used is the assumption that the refraction of light is negligible. This allows an implementation of a computationally efficient ray-tracing algorithm that does not need to change the orientation of the light rays during their passage through the numerical domain. This simplification is found to be negligible for the conditions achievable in the wind tunnel tests in TMK. However, this simplification may be relevant in case of high optical density gradients and/or wide test sections, where the refraction of light changes the light ray paths significantly.

Apart from this simplification, the approach for generating computed schlieren images rebuilds the physical principle of the schlieren technique.

### 5.3. Boundary Conditions

The cold flow in combination with the low densities in the test section allow utilizing the perfect gas simplifications in the numerical rebuilding. For the given Reynolds number $Re \approx 0.5 \cdot 10^6$, a laminar boundary layer is assumed.

The computational resources available to the authors are limited, so a stationary modelling of the flow is necessary. As the numerical investigations are intended to support the interpretation of the experimental results, the main interest is the flow before the shoulder. The aft flow has a negligible influence on the forebody flow in the supersonic environment. The stationary modelling is therefore considered acceptable despite the problems in the aft flow.

The simulations show a non-stationary nature in the wake region. This results in the simulations not converging to a stable solution within a reasonable number of iterations. Instead, the aft flow shows an oscillating behaviour. This is contradictory to the stationary approach. The resulting flow and the aerodynamic coefficients vary accordingly with the number of iterations. These stability issues lead to a fluctuation of the base pressure for the whole angle of incidence range. The degree depends on the capsule orientation. Aerodynamic coefficients that include the base pressure ($C_A$ and $C_{p_B}$) reflect this. The same issue was observed in the laminar simulations of the previous study.

### 5.4. Numerical Results

The trends of the aerodynamic coefficients at $M = 1.5$ derived from the numerical results agree with the measured data for all three capsule shapes (Figure 9). The numerical data points of the fore body force coefficient $C_{A_{FB}}$ match the experimental curve. This indicates that the numerical rebuilding of the tests captures the major flow phenomena to a sufficient degree.

The experimental $C_{A_{FB}}$ values are calculated from the measured axial force coefficient $C_A$ by subtraction of $C_{p_B}$. The latter is derived from the base pressure measurement (approximated by the static pressure inside the shell). Thus, the agreement between numerical and experimental fore body force coefficient proves that the approach to approximate the base pressure is reasonable and the corresponding values are accurate.

The issues with the convergence and stability of the base flow in the numerical simulations show in the fluctuation of the base pressure coefficient $C_{p_B}$. Also, the numerical and experimental values fit well for low angles of incidence, but deviate at higher angles.

The axial force coefficient $C_A$ includes the base pressure coefficient, so the fluctuations and offset can be observed in this coefficient, too. The normal force coefficient $C_N$ and the pitching moment coefficient $C_m$ are less sensitive to a correct capturing of the aft flow and they coincide well with the measured data. This is explained by the fact that the surface pressure is significantly higher on the front of the capsule and the numerical issues only concern the rear pressure distribution.

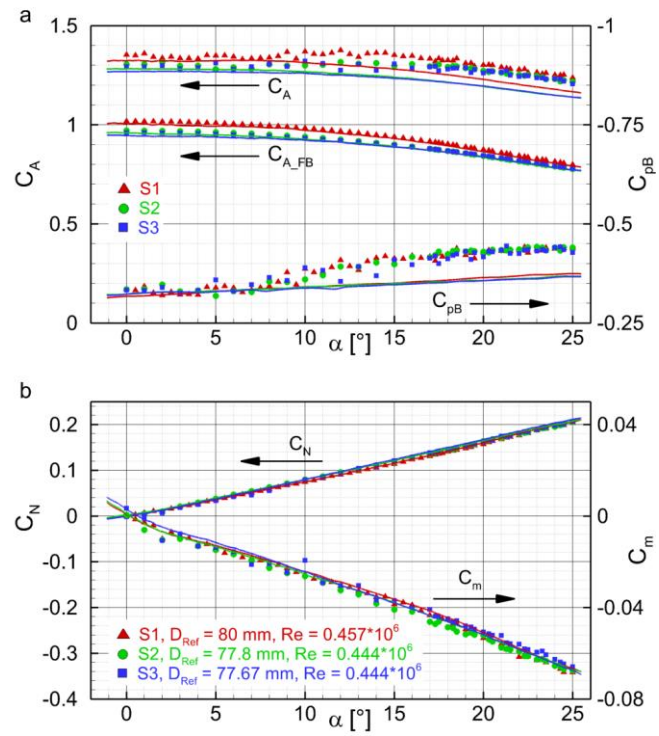


**Figure 9: Aerodynamic coefficients at $M = 1.5$ derived from numerical results (symbols) compared to wind tunnel measurements (solid lines)**

### 5.5. Experimental and numerical visualisations

Figure 10 shows experimental and numerical schlieren images of the three capsule models. The angle of incidence in these images goes from ~17.3 to ~21.3 degrees and is given in the top left of each image. The numerical simulations always use the same angle, but the orientation in the experimental images varies a bit, depending on the availability of Schlieren images. Justified by the relatively slow sweeping rate, stationary conditions can be assumed. The non-stationary character of the wake flow observed in the numerical simulations is visible in the numerical schlieren pictures.

The experimental setting of the schlieren optic differed slightly between the test campaigns, but a reduction of the shock strength can be derived when the capsule shape is changed from S1 to S2 or S3. Also, a strong dependency of the shock system structure on the shape and the incidence angle can be observed.

At the incidence angle $\alpha = \sim 17.3°$, a dark region around the leeward sphere-cone-transition is visible in case of the S1 shape in both, the experimental and the numerical schlieren image. The shock starts to form, but structures cannot yet be resolved. This is explained by the low strength of the shock in combination with its three-dimensional structure. At this angle, the symmetric recessed shape S2 already experiences the onset of a multiple-interaction (see [7] or [3] for the different interaction types) with several weak successive shocks. This phenomenon is typical for the interaction of a laminar boundary layer with a near normal shock wave. The system is visible in the experimental image and also reproduced to a certain extent in the numerical simulation. In contrast, the asymmetric shape S3 does not experience any visible formation of a shock system at that orientation.

With a further increasing incidence angle, the multiple-interaction shock system also forms on S1 ($\alpha = \sim 18.3°$) and shows the maximum extension around $\alpha = \sim 19.3°$. The shocks appear to be slightly smeared, which is typical for this interaction type. Compression waves ahead of the shocks contribute to this. The three-dimensional flow and the curved shape of the shocks in combination with the line-of-sight nature of the schlieren imaging technique are also relevant. In the experiment, the initial and at least three successive shocks are visible. The numerical schlieren image only shows the initial and one successive shock wave. On S2, increase of the incidence angle leads to a further development of the multiple-interaction shock system. The maximum extension is already reached around $\alpha = \sim 18.3°$ with two successive shocks being visible in the experiment and one in the numerical simulation. In contrast, no clear shock structures develop on S3 at that incidence angle, neither in the experiment nor in the simulation.

The flow around S1 retains elements of the multiple-interaction at $\alpha = \sim 20.3°$. The higher incidence angle leads to a further re-acceleration and an increased pre-shock Mach number on the lee side. The compression waves ahead of the initial shock merge into an oblique shock with increased strength, which shows in a higher gradient (darker grey level) in the schlieren image. This weakens the second foot of the $\lambda$-shaped shock. Downstream the initial shock, the flow is re-accelerated and one subsidiary shock wave follows. Compared to the previous case, the deceleration by the initial shock is higher. Accordingly, the re-acceleration takes longer and the distance to the subsidiary shock increases. The shock structure is well reproduced in the numerical simulation with a slightly different shape of the initial shock.

The flow structure is highly three-dimensional and there is a discontinuity in the second derivative of the surface at the sphere-cone-transition. Regard that the shock changes its orientation with increasing angle of incidence, thereby moving downstream. However, the front foot of the shock remains attached to the surface discontinuity at all angles in the experimental and numerical images. This might force the initial shock to adapt a $\lambda$-shape, while without the discontinuity it would be an oblique shock positioned further downstream.

The last schlieren image for S1 shows the capsule at $\alpha = \sim 21.3°$. The photograph implies a single oblique shock wave with the origin near the sphere-cone-transition and a slight S-shape. A similar shock wave results in the numerical schlieren image of that case, but a closer look into simulation details at this condition reveals that the shock is still a $\lambda$-shock about to becoming oblique in the area close to the symmetry axis. The second foot is not resolved in the line-of-sight schlieren visualisation.

A shock system of two successive $\lambda$-shocks is observed on S2 at an incidence angle of $\alpha = \sim 19.3°$. The structure is comparable to that on S1 at a higher angle, but the oblique part of the initial shock seems to be weaker. The same accounts for the $\lambda$-structure of the second shock. At this condition, the flow phenomena are nicely reproduced in the numerical simulation with a slight underestimation of the second shock wave. On S3, again, no clear structures are visible at that incidence angle.

At $\alpha = \sim 20.3°$, one shock with a $\lambda$-shape remains visible in the schlieren image of S2 whereby the $\lambda$-part appears quite weak. At a further increased angle of $\alpha = \sim 21.3°$, the oblique part of the shock remains at rest while the normal part gets diffuse. At that condition, the schlieren image shows additional disturbances of the flow field near the capsule surface ahead of the $\lambda$-shock.

The observations on the flow field of S2 are supported by the numerical simulations that reproduce well the flow structures at both conditions, including the additional disturbances. From analysis of the density gradient (not shown), these are revealed as a system of successive shock waves that occur around the centre line of the flow. Due to the line-of-sight character, they are rarely visible in the schlieren visualisations.

The non-symmetric shape S3 shows a diffuse density gradient with a potential $\lambda$-shape that might be followed by a second weak compression wave at $\alpha = \sim 20.3°$. At $\alpha = \sim 21.3°$ one diffuse shock wave is visible, that is now steeper and extends further into the far field of the capsule. The diffuse shock system is also found in the numerical simulation of the shape at the two angles. The determined flow structures match quite well with the experiment.

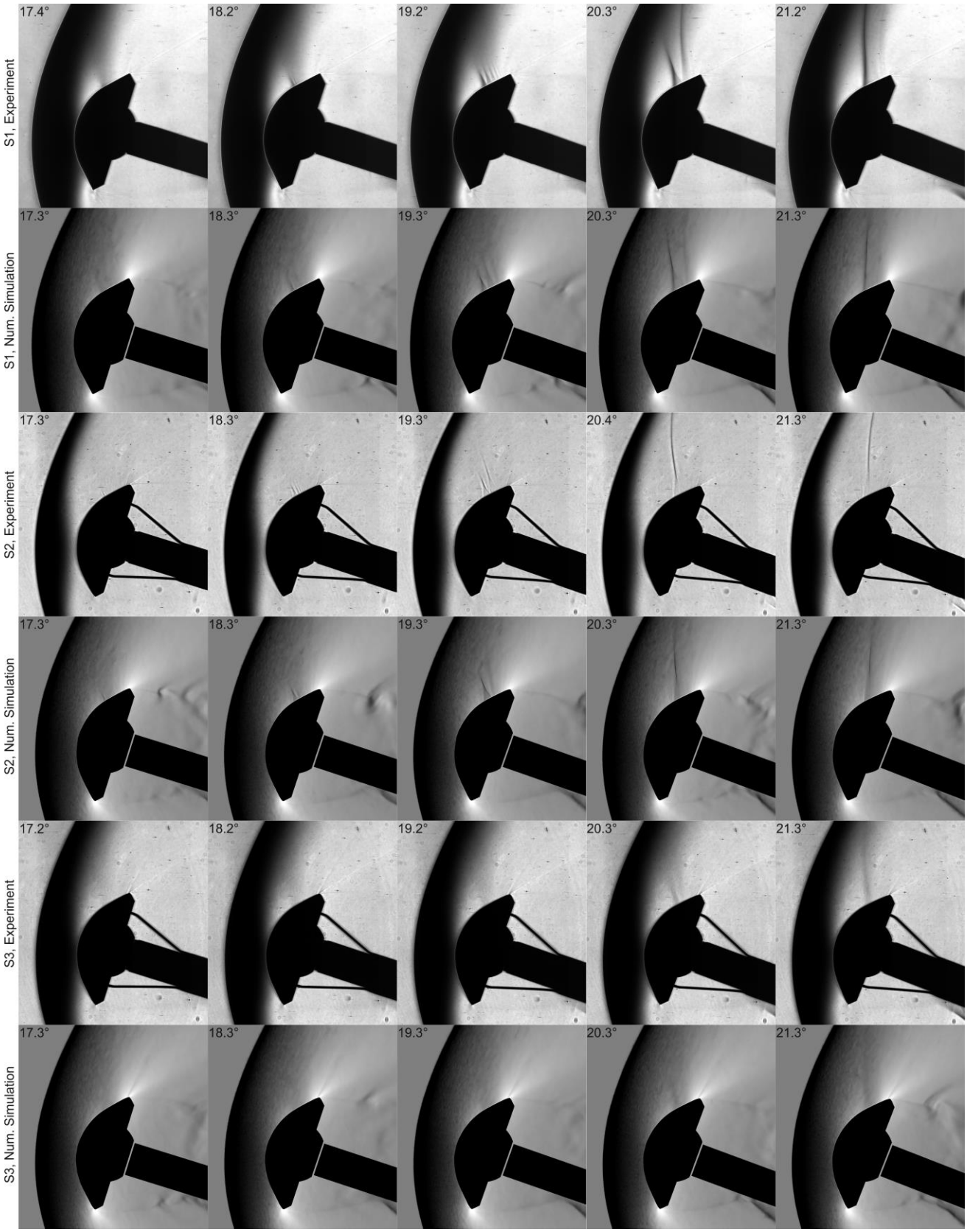


**Figure 10: Experimental and numerical schlieren images, $M = 1.5$, $Re \approx 0.5 \cdot 10^6$**

## 6. CONCLUSION

Three different entry capsule aero shapes were investigated experimentally and numerically in this study. The baseline shape S1 represents the original MarcoPolo-R aero shape and a virgin capsule. The other geometries S2 and S3 were derived from recession measurements on Camphor models exposed to hypersonic flow in the H2K wind tunnel at $M = 6.0$, $Re = 5.4 \cdot 10^6$ and $\alpha = 0°$ and $\alpha = 5°$, respectively. Force and moment measurements were performed on the three geometries in TMK wind tunnel and static stability was proven for all three shapes in the investigated Mach number range.

At an inflow Mach number of $M = 1.5$, systems of shock waves form on the leeward sides of the inclined S1 and S2 capsules. These systems change with the incidence angle. The shock systems were visualised using schlieren imaging. Within numerical simulations, the flow structure and the aerodynamic coefficients could be well reproduced. Flow structures were found to strongly depend on the capsules' shape and the incidence angle. As the impact area of the leeward shock system on the capsules' surface is relatively small, the observed difference in the shock systems have little impact on the aerodynamic coefficients of the capsules.

Despite the complex and three-dimensional flow, it was possible to rebuild the shock boundary layer interaction fairly well in the numerical simulations using a laminar boundary layer. The finite computational resources available limited the numerical investigations to stationary simulations. The boundary layer development along the surface of capsule S1 is influenced by the discontinuity, which affects the formation of the shock systems. As the other aero shapes were defined by a measured material recession in aerodynamic wind tunnel tests, it is likely that discontinuities on the surface diminished. The observed shock wave boundary layer interaction structures on these capsules support this assumption.

The laminar boundary conditions proved to be suitable for a fairly good reproduction of the secondary shock system on the capsule. Transition to turbulence is not observed. The aerodynamic coefficients could be rebuilt, too. For future research, investigation of the dynamic aspects of the observed shock-boundary layer interaction and improvement of the numerical simulations are recommended.


### Acknowledgements

This work was partially performed under ESA contract 4000122733/17/NL/KML. The view expressed herein can in no way be taken to reflect the official opinion of the European Space Agency. The authors would like to thank ESA for the support of this work. The financial support of the DLR's programme directorate for space research and technology for the remaining part of the study is also acknowledged. Further thanks go to Martin Achner and Daniel Habegger for their support in performing the wind tunnel tests in TMK.


## 7. REFERENCES


[1] **Clopeau, E.; Tran, P.; Ferracina, L.; Marraffa, L.:** *MarcoPolo-R ERC Dynamic Stability Characerization: Study Logic*. 8th European Symposium on Aerothermodynamics, Lisbon, Portugal, 2-5 March, **2015**.

[2] **Neeb, D.; Seltner, P.; Gülhan, A.; Ferracina, L.:** *Modelling capsule stability accounting for shape change*. International Conference on Flight Vehicles, Aerothermodynamics and Re-entry Missions & Eingineering, Monopoli, Italy, 30 September - 3 October, **2019**.

[3] **Gawehn, T.; Schleutker, T.; Gülhan, A.:** *Capsule aerodynamics and shock-wave boundary layer interaction (SBLI) in supersonic and transonic flow.* Experiments in Fluids, Vol. 63, No. 3, ISSN 1432-1114, pp. 61, 2022/03/21, **2022**.

[4] **Seltner, P. M.; Neeb, D.; Gülhan, A.; Ferracina, L.:** *Experiments on the static stability of a changing capsule shape in hypersonic flow*. 2nd International Conference on Flight Vehicles, Aerothermodynamics and Re-entry Missions & Engineering, Heilbronn, Germany, 19 - 23 June, **2022**.

[5] **Schwamborn, D.; Gerhold, T.; Heinrich, R.:** *The DLR TAU-code: Recent Applications in Research and Industry*. ECCOMAS, Delft, The Netherlands, 4-8 September, **2006**.

[6] **Langer, S.; Schwöppe, A.; Kroll, N.:** *The DLR Flow Solver TAU - Status and Recent Algorithmic Developments*. 52nd Aerospace Sciences Meeting, National Harbor, Maryland, USA, 13-17 January, **2014**.

[7] **Houghton, E. L.; Carpenter, P. W.; Collicott, S. H.; Valentine, D. T.:** *Aerodynamics for engineering students. - 6th ed.*, Lewis, E. (Ed.), Butterworth-Heinemann, Elsevier, ISBN ISBN 978-0-08-096632-8, **2013**.